Journal of Astronomical Telescopes, Instruments, and Systems

AstronomicalTelescopes.SPIEDigitalLibrary.org

In-flight performance of the soft x-ray spectrometer detector system on Astro-H

Frederick S. Porter
Kevin R. Boyce
Meng P. Chiao
Megan E. Eckart
Ryuichi Fujimoto
Yoshitaka Ishisaki
Caroline Anne Kilbourne
Maurice A. Leutenegger
Daniel McCammon
Kazuhisa Mitsuda
Kosuke Sato
Hiromi Seta
Makoto Sawada
Gary A. Sneiderman
Andrew E. Szymkowiak
Yoh Takei
Makoto S. Tashiro
Masahiro Tsujimoto
Tomomi Watanabe
Shinya Yamada

Frederick S. Porter, Kevin R. Boyce, Meng P. Chiao, Megan E. Eckart, Ryuichi Fujimoto, Yoshitaka Ishisaki, Caroline Anne Kilbourne, Maurice A. Leutenegger, Daniel McCammon, Kazuhisa Mitsuda, Kosuke Sato, Hiromi Seta, Makoto Sawada, Gary A. Sneiderman, Andrew E. Szymkowiak, Yoh Takei, Makoto S. Tashiro, Masahiro Tsujimoto, Tomomi Watanabe, Shinya Yamada, "In-flight performance of the soft x-ray spectrometer detector system on Astro-H," *J. Astron. Telesc. Instrum. Syst.* **4**(1), 011218 (2018), doi: 10.1117/1.JATIS.4.1.011218.

SPIE.

In-flight performance of the soft x-ray spectrometer detector system on Astro-H

Frederick S. Porter,[a,*] Kevin R. Boyce,[a] Meng P. Chiao,[a] Megan E. Eckart,[a] Ryuichi Fujimoto,[b] Yoshitaka Ishisaki,[c] Caroline Anne Kilbourne,[a] Maurice A. Leutenegger,[a] Daniel McCammon,[d] Kazuhisa Mitsuda,[e] Kosuke Sato,[f] Hiromi Seta,[c] Makoto Sawada,[g] Gary A. Sneiderman,[a] Andrew E. Szymkowiak,[h] Yoh Takei,[e] Makoto S. Tashiro,[i] Masahiro Tsujimoto,[e] Tomomi Watanabe,[a] and Shinya Yamada[c]

[a]National Aeronautics and Space Administration, Goddard Space Flight Center, Greenbelt, Maryland, United States
[b]Kanazawa University, Department of Physics, Kanazawa, Ishikawa, Japan
[c]Tokyo Metropolitan University, Department of Physics, Hachioji, Tokyo, Japan
[d]University of Wisconsin, Department of Physics, Madison, Wisconsin, United States
[e]Japan Aerospace Exploration Agency, Institute of Space and Astronautical Science, Sagamihara, Kanagawa, Japan
[f]Tokyo University of Science, Department of Physics, Shinjuku-ku, Tokyo, Japan
[g]Aoyama Gakuin University, Department of Physics and Mathematics, Sagamihara, Kanagawa, Japan
[h]Yale University, Department of Physics, New Haven, Connecticut, United States
[i]Saitama University, Department of Physics, Saitama, Japan

Abstract. The soft x-ray spectrometer (SXS) instrument was launched aboard the Astro-H (Hitomi) observatory on February 17, 2016. The SXS is based on a high-sensitivity x-ray calorimeter detector system that has been successfully deployed in many ground and suborbital spectrometers. The instrument was to provide essential diagnostics for nearly every class of x-ray emitting objects from the atmosphere of Jupiter to the outskirts of galaxy clusters, without degradation for spatially extended objects. The SXS detector system consisted of a 36-pixel cryogenic microcalorimeter array operated at a heat sink temperature of 50 mK. In preflight testing, the detector system demonstrated a resolving power of better than 1300 at 6 keV with a simultaneous bandpass from below 0.3 keV to above 12 keV with a timing precision better than 100 μs. In addition, a solid-state anticoincidence detector was placed directly behind the detector array for background suppression. The detector error budget included the measured interference from the SXS cooling system and the spacecraft. Additional margin for on-orbit gain stability and on-orbit spacecraft interference were also included predicting an on-orbit performance that meets or exceeds the 7-eV FWHM at 6-keV requirement. The actual on-orbit spectral resolution was better than 5 eV FWHM at 6 keV, easily satisfying the instrument requirement. Here, we discuss the actual on-orbit performance of the SXS detector system and compare this to performance in preflight testing and the on-orbit predictions. We will also discuss the on-orbit gain stability, additional on-orbit interference, and measurements of the on-orbit background. [DOI: 10.1117/1.JATIS.4.1.011218]

Keywords: x-ray astrophysics; x-ray spectroscopy; x-ray detectors.

Paper 17046SSP received Aug. 18, 2017; accepted for publication Jan. 19, 2018; published online Feb. 20, 2018.

1 Introduction

The soft x-ray spectrometer (SXS) instrument[1] is a broadband nondispersive x-ray spectrometer (XRS) that was launched on February 17, 2016, as part of the Astro-H x-ray observatory. The Astro-H observatory and the SXS instrument performed extremely well, satisfying all of their requirements up until communication with the observatory was lost[2] on March 26, 2016. During the short life of the observatory, extensive performance data and several science observations[3] were obtained with the SXS instrument giving an excellent baseline to compare its performance with predictions and data obtained during ground testing and ground calibration. The performance of the detector subsystem, more generally referred to as the focal plane assembly (FPA), will be discussed in this document. The performance of the dewar, adiabatic demagnetization refrigerator (ADR), electronics, and operations are discussed elsewhere.[4–9] However, for completeness, a brief description of the instrument is presented here.

The SXS is a nondispersive XRS based on cryogenic x-ray microcalorimeters. An x-ray microcalorimeter detects the energy of an incident x-ray by measuring the heat-of-absorption in a low heat capacity absorber using a high-sensitivity thermometer. In principle, very high resolving powers can be achieved, including resolving powers of over 3000 at 6 keV and over a substantial bandpass.[10] The pixels in an array of microcalorimeters are also spatially distinct, in that, with a suitable telescope, each pixel is its own spatially independent spectrometer. Thus, this type of instrument is well suited for observing extended objects, such as galaxy clusters, and supernova remnants without the spatial–spectral confusion associated with slitless dispersive spectrometers, such as those on XMM-Newton and Chandra.

The SXS detector is a 36-pixel microcalorimeter array inherited from the XRS program for Suzaku,[11] but with 85% larger

*Address all correspondence to: Frederick S. Porter, E-mail: Frederick.S.Porter@nasa.gov

area than XRS and new, low heat capacity absorbers.[12] The array is organized as a square 6×6 pixel imager of close-packed pixels on a ~0.84-mm pitch with a total field of view of 3×3 arc min. Close behind the array is a low-voltage ionization anticoincidence detector (ACD) to exclude events associated with high-energy cosmic rays, significantly reducing the instrument background.[12] The detector array and ACD are mechanically supported and thermally isolated within an FPA that also houses detector electrical bias components and the first stage amplifiers. The detector system is cooled to 50 mK by an ADR. The FPA is mounted on a long-life (estimated post-launch to be >4 years on-orbit)[6] liquid helium tank that is also the exhaust heat sink for the ADR. The liquid helium tank is supported and thermally shielded by a series of vapor and mechanically cooled shells within the SXS cryostat. A series of five mechanical coolers provides the majority of the thermal isolation from the dewar vacuum shell. There is also an additional ADR stage that provides redundancy for the liquid helium system and can indefinitely extend SXS operations even after the liquid helium is exhausted.[13] A majority of the SXS FPA design is to isolate the thermally, mechanically, and electrically sensitive detector system from the intricate SXS cooling system, as well as the complex Astro-H spacecraft. The success of the FPA design is demonstrated by the fact that the SXS performance is little changed on-orbit compared to preintegration testing of the FPA and is well within the performance requirements. Note that details of the pulse-processing algorithm, including the on-orbit performance of event-grading, triggering, and timing performance, are described in detail by Ishisaki et al.[5]

2 Focal Plane Assembly

The SXS FPA is described more fully by Chiao et al.[14] and Porter et al.[15] but is described briefly here to set the stage for the discussion that follows. An overview of the subsystem is shown in Fig. 1 with most of the major subassemblies labeled. The FPA is composed of modular subassemblies for ease of integration, including a 50-mK detector housing, two 19-channel (a 20th is installed but not used) junction field-effect transistor (JFET) front-end amplifier assemblies, and a bias assembly. The FPA housing (midsection) is thermally attached to the SXS helium tank at a temperature around 1.1-K in-flight. The detector housing that contains the detector array, the ACD, the first stage infrared blocking filter, the load resistors, and the four control and monitor thermometers is suspended from the midsection using tensioned Kevlar threads and has a resonance frequency above 300 Hz. The detector housing is attached to the ADR 50-mK cooler using annealed high-purity copper foils. The detectors are biased through voltage dividers in the bias module and kept in nearly constant current through separate 130-MOhm Si/Cr load resistors inside the detector housing. The 30-MOhm (under bias) detectors are read out using a cold (130 K) JFET source follower to reduce microphonic sensitivity due to stray capacitance. The ACD is a low-voltage (6 V) silicon ionization detector placed close behind the main detector array. It is biased through two 5-MOhm load resistors in parallel and read out with redundant JFET channels identical to the main detector array.

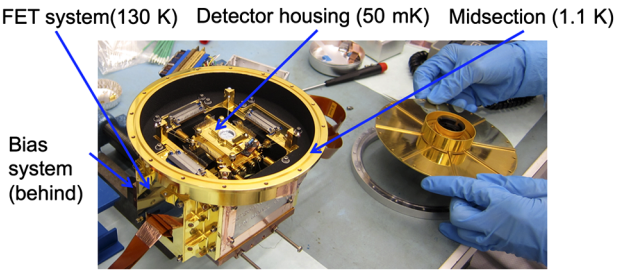

Fig. 1 The SXS FPA during final integration before assembly into the SXS instrument. The major components are labeled.

The JFET subsystems are organized in two identical modules and are again divided into two quadrants each for instrument segmentation. The four quadrants are largely independent although there is a shared thermometer and heater in each of the two JFET modules. The JFETs are controlled at 130 K within about 5 cm of the 50-mK detector array, and a substantial amount of the FPA complexity is to manage the thermal interference between these modules while keeping all the electrical connections tensioned with resonance frequencies >5 kHz to minimize microphonics.

The FPA subsystem was constructed, tested, and calibrated before integration with the 50-mK ADR and then with the rest of the SXS instrument.

3 In-Flight Performance

The primary differences between the in-flight performance of the SXS focal plane and its performance on the ground are additional sources of in-band noise and our ability to reconstruct the detector gain as a function of time. Both of these effects contribute to the resolving power of the spectrometer. In-band noise is the most obvious contributor since it directly affects our ability to reconstruct the incident photon energy from the detector response. However, since the calorimeter array consists of thermal detectors, controlling and reconstructing the detector gain are also critically important and consist of many components, including detector housing temperature, thermal radiation field, electronic gain temperature coefficients, and the JFET temperature (weakly). There are also nonideal effects that contribute to the detector gain, including conducted loading of the 50-mK control thermometers and differential detector sensitivity to the ambient thermal radiation field. We will discuss many of these effects here.

The result, though, is that the SXS, and specifically the SXS FPA, performed very similarly in-flight as on the ground. The primary requirement on the SXS, which distinguishes it from all other orbital XRSs, is an energy resolution of <7 eV at 6 keV. The detailed noise budget and allocations are given by Kelley et al.,[1] but the final budget prior to integration of the SXS onto the Astro-H spacecraft is shown in Fig. 2 along with measurement milestones during final integration and on-orbit. The preintegration results are shown for two event grades (high and mid) that correspond to the x-ray pulse spacing resulting from moderate pile-up and in two operating modes: with cryogen and in SXS's contingency mode of operating without cryogen. Ground testing showed no appreciable difference in performance between the SXS's two operating modes.

The SXS detector system performed marginally worse after spacecraft integration and on-orbit compared to SXS instrument testing as shown in Fig. 2, but still well within its requirement. Nearly, the entire margin in the error budget assigned to on-orbit degradation remained unused in-flight. The small degradation in performance is largely a result of interference from the spacecraft attitude control system that leads to in-band electrical interference as discussed in Sec. 3.3.

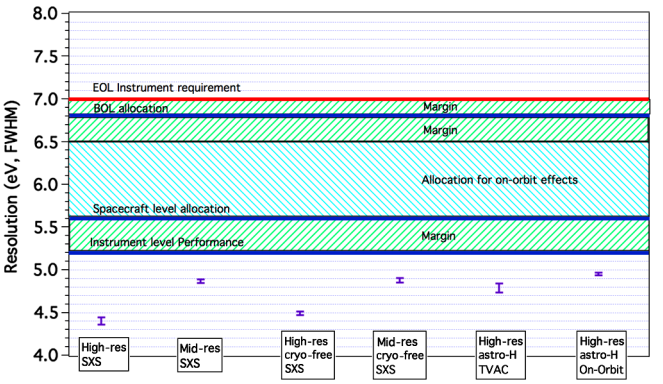

Fig. 2 Composite energy resolution of the 35-pixel SXS detector system at 6 keV prior to integration, during spacecraft thermal vacuum testing (TVAC), and on-orbit. Also shown is a summary of allocations and margins from the SXS system noise budget that benchmarks the detector system against the 7-eV requirement. The difference between high/mid grades and standard versus cryogen-free (cryo-free) mode are discussed in the text.

3.1 *JFET Performance*

The JFET subsystem uses a single InterFET SNJ14AL16 per detector channel to reduce the detector impedance, under bias, from ~30 MOhm to 1 to 2 kOhm in order to drive the long cable run out of the SXS dewar without microphonic interference. The on-orbit JFET noise spectra are shown in Fig. 3. The noise spectra were recorded before the detectors were cooled to 50 mK and include the Johnson noise of the <100-kOhm detectors at 1.2 K and the SXS amplifier noise (1 to 2 nV/sqrt Hz) but are dominated by the 6- to 7-nV/sqrt Hz JFET noise. The noise spectra were calculated on-board the spacecraft by the SXS pulse shape processor.[5] Note that we do not show the equivalent preflight noise spectra since they are indistinguishable from what is shown in Fig. 3.

The amount of power used to maintain the JFETs at 130 K is a critical indicator of the on-orbit performance of the JFET subsystem. The JFET modules have a two stage Kevlar isolation system that shunts most of the 13-mW total dissipated power to an intermediate 22-K heat sink cooled by the SXS inner vapor cooled shield (IVCS) (also cooled by the SXS shield cryocoolers). The amount of power required to heat the JFET modules and the stability of the control are very sensitive to the mechanical integrity of the JFET assemblies, the stability of the 22-K heat sink, the amount of gas loading in the dewar, and the performance of the control electronics. The dissipated power as a function of time over several hours on-orbit is shown in Fig. 4. Again we are not showing the ground performance since the difference would not be visible in the figure. The on-orbit dissipated power is 0.50% higher (box A) and 0.53% higher (box B) than the values during preflight testing. This is consistent with the 2-K lower IVCS heat sink temperature on-orbit. The controller noise of <20-μW rms is identical to the ground performance. Temperature regulation over the time interval, as shown in Fig. 4, is 11-mK rms (box A) and 22-mK rms (box B). The peak-to-peak values are below 200 mK even over the large 7-h baseline, well within the 500-mK p–p requirement. Thus, all indications are that the JFET assemblies in the FPA performed as expected on-orbit.

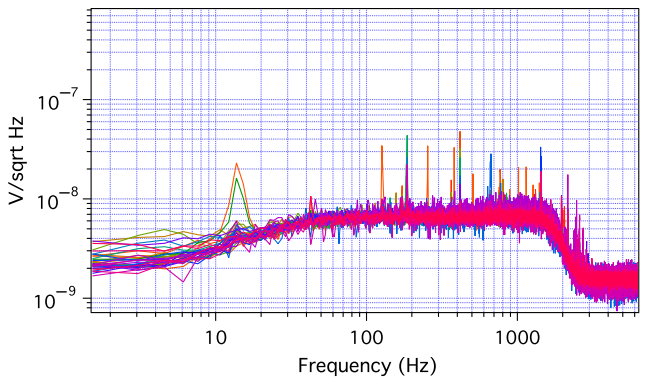

Fig. 3 On-orbit detector channel noise spectra with the detectors warm at ~1.2 K. Each trace is a different detector. The noise is dominated by the on-board JFET amplifiers. The preflight noise spectra are not plotted as they are indistinguishable from the in-flight spectra. The detector electronics chain includes a 30-Hz single-pole high-pass filter and an 8-pole antialias filter at ~1.5 kHz. The bump at ~14 Hz is interference from the SXS Stirling cycle cryocoolers and is most pronounced on two detector channels that share a common return signal. We note that about 12 h later, channel 35 started to exhibit some $1/f$ noise that is discussed later in the text.

3.2 *50-mK Control Thermometry*

The detector housing contains four Lakeshore Cryotronics Germanium Resistance Thermometers for control and monitoring the detector heat sink temperature at 50 mK. The details can be found in the work by Chiao et al.[14] The thermal stability of the detector housing directly affects the detector gain since the detectors have a gain coefficient at 50 mK of about 0.2 eV/μK at 6 keV. The SXS contains multiple on-board calibration sources to measure and correct long-term gain drift, but fast temperature fluctuations cannot be removed using the calibration sources or during pulse processing since the ~10-s thermal time constant of the detector housing is out-of-band for the detector electronics (see Fig. 3). Thus, the stability of the detector housing and the sensitivity of the control thermometers are primary design drivers for the FPA.

Two of the four detector housing thermometers are read out by the SXS electronics. The other two thermometers are dark spares that can be switched in to the two readout channels as necessary (all four performed nominally on-orbit). One of the

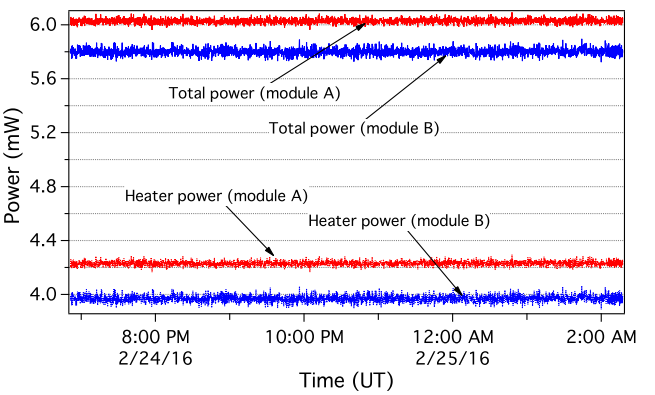

Fig. 4 Power dissipated in each of the two JFET modules (A and B) to maintain the JFETs at 130 K on-orbit. The lower curves are the module heater powers and the upper curves are the total dissipated power that also includes the power dissipated in the JFETs themselves. The JFET modules require ~0.5% higher power on-orbit due to a 2 K lower IVCS heat sink temperature.

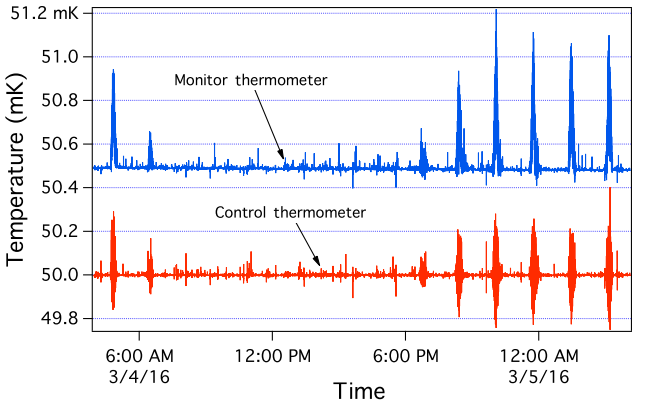

Fig. 5 Detector housing control and monitor thermometer temperatures on-orbit over a 24-h period. The large excursions to the left and right of the figure are during passages through the SAA. These regions are excluded from the science data. The smaller spikes are the result of cosmic rays interacting with the thermometer.

two readout channels is used for closed-loop control of the detector housing temperature by feeding back to the superconducting magnet that controls the field on the stage 1 ADR salt pill.[6] The other thermometer channel is used as a monitor. The detector housing temperature during in-flight closed-loop control is shown in Fig. 5 for a 24-h period. The germanium sensor element has a volume of a few mm^3 and is thus susceptible to heating due to cosmic rays. The large excursions to the left and right of the figure are due to particle heating events associated with passage through the South Atlantic Anomaly (SAA). The detectors themselves also see a large increase in particle background associated with the SAA and these regions are generally excluded from the science analysis. Outside of the SAA, the thermometers are also sensitive to individual cosmic rays interacting directly with the thermometers.

In Fig. 6, we show a zoomed-in region of a cosmic ray interacting with the control thermometer. This only affects the temperature of the thermometer itself, but the overcontrol (reaction) of the temperature controller has a subsequent affect on the detector housing temperature as can be seen on the monitor thermometer. Since the housing temperature is affected by the overcontrol, this has an effect on the detector gain and, if not removed in the analysis, on the detector resolution. To examine this effect, we used the same 24-h period as shown in Fig. 5 and

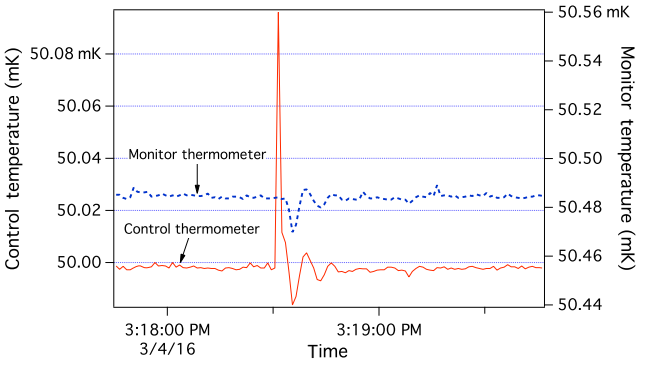

Fig. 6 A 100-μK spike on the control thermometer due to a cosmic ray that causes a ~20-μK overcontrol of the detector housing as shown by the monitor thermometer. These events have a small impact on the instrument performance as discussed in the text.

looked at the resolution of the array calibration pixel. The detector array contains a calibration pixel identical to the main array, but placed a couple of millimeters to the side, outside of the instrument aperture. The calibration pixel is continuously illuminated by a highly collimated internal ^{55}Fe radioactive x-ray source producing 5.9- and 6.5-keV x-rays.

For this particular 24-h period, the average calibration pixel resolution was 4.77-eV FWHM at 5.9 keV, including all high-resolution events, but excluding the SAA. We then excluded a 20-s period after each cosmic ray event >5 μK on the control thermometer. This introduced a ~5% dead time. The impact on the detector performance, however, was minimal. The energy resolution improved by 0.06 ± 0.04 eV FWHM, and the line centroid energy was displaced by $7.4 \times 10^{-3} \pm 1.5 \times 10^{-2}$ eV at 5.9 keV. In the nominal SXS processing, this effect is neglected, and no cuts for cosmic ray events in the thermometry are made in the analysis. Cosmic ray effects in the thermometry are a function of the volume of the thermometer, its heat capacity, and its heat sinking. The RuO_2 thermometers used on XRS[11] showed much less of this effect due to their much smaller active volume but also had ~5× lower sensitivity. While the cosmic ray interference has only a minor effect on SXS performance, the effect on the instrument could be completely mitigated by a more sophisticated control algorithm since the heating is in the thermometer and not in the detector housing.

Finally, it is clear from Fig. 5 that the control and monitor thermometers systematically differ by about 0.5 mK. This is not a calibration artifact. The actual dispersion of the four thermometers at 50 mK is <0.05 mK as measured during a careful calibration verification of the thermometers prior to SXS integration. The systematic dispersion of the two thermometers is the result of inadequate heat sinking in the detector housing. The SXS detector housing is small at $4.0 \times 3.3 \times 1.2$ cm and weighs only ~90 g. It thus has limited volume for heat sinking the thermometer wires, which have a conducted heat load on the thermometer itself. The thermometers are connected to the 1.1-K FPA heat sink through tensioned 18-μm-diameter CuNi-coated NbTi electrical leads, ~1-cm long. In the detector housing, the BeCu thermometer wires are wound and potted inside the housing as described by Chiao et al.[14] to improve their heat sinking, but this was not completely successful. Through an analysis of the detector gain, the control thermometer is actually 0.5 mK higher than the detector housing temperature because of this effect. From Fig. 5, the monitor thermometer has a lower conductance to the heat sink than the control thermometer leading to the systematic offset as well as the increased temperature during SAA passage relative to the control thermometer. Finally, since the thermometer temperature is affected by the ~1.1-K FPA heat sink temperature (the SXS helium tank), variations of this temperature will affect the detector gain, especially during the initial cool down on-orbit. We discuss this in Sec. 3.4.

3.3 *In-Band Detector System Noise*

As shown in Fig. 2, the detector resolution became slightly worse after the SXS instrument was integrated onto the spacecraft. The degradation is due to interference from the spacecraft attitude control system, specifically the momentum wheels and the magnetic torquer system used by the spacecraft to shed excess angular momentum. The interference is likely mechanical and electrical, respectively, and shows up in the detector noise spectrum at the rotation rate of the momentum wheels and the pulse width modulation frequency of the magnetic

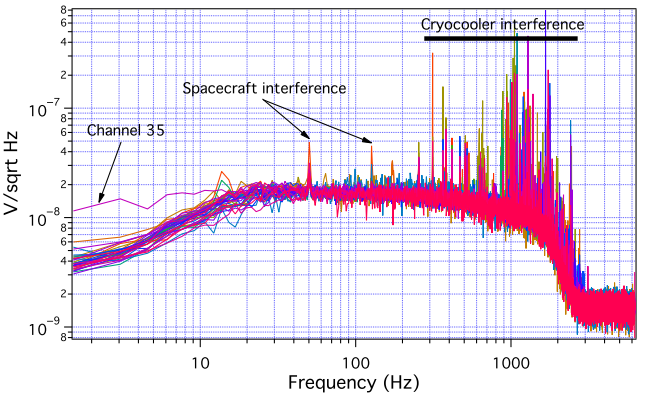

Fig. 7 In-flight detector noise spectra for all 36-detector channels, with some noise sources labeled. The right-hand edge is the Nyquist frequency for the 12.5-k sample/s sample rate.

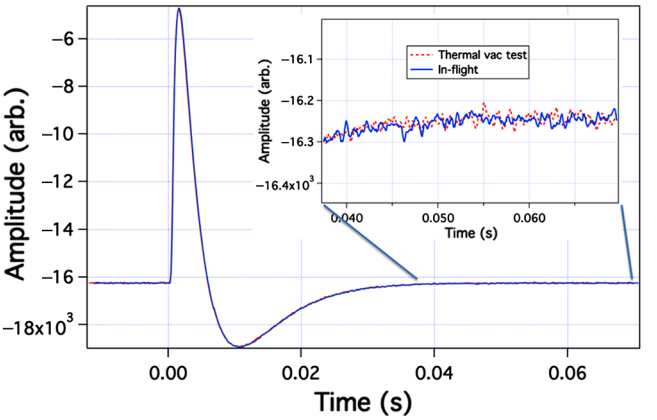

Fig. 8 Two single x-ray events at 6 keV measured with the SXS, one from spacecraft TVAC and the other taken on-orbit during the first week of observation. Note that in the time domain, there is no easily perceptible difference, which translates into the very similar performance measured in-flight.

torquer system, although the exact coupling mechanism is not known. This is discussed in more detail by Eckart et al.[16]

The in-flight detector noise spectra are shown in Fig. 7 for the detectors at their 50-mK operating temperature. This can be compared to the warm detector case that is dominated by JFET noise and is shown in Fig. 3. With the detectors cold, several additional features are apparent. The broadband continuum represents the intrinsic detector noise (Johnson noise + phonon exchange noise).[17] The forest of lines at high frequencies is the residual interference from the cryocoolers after a mechanical vibration isolation system was incorporated into the SXS design. The high-frequency cryocooler interference has no impact on performance since the pulse-power band of the detectors only extends up to about 200 Hz. The interference only affects triggering and is well below the lower level discriminators used on the SXS (<100 eV). Without the cryocooler mechanical isolators, there is considerably more interference, including nonstationary dissipative heating in the suspension of the detector housing. This is discussed by Takei et al.[9] In ground testing and on-orbit, the mechanical isolators are 100% effective in eliminating any performance degradation. The exceptions are channels 19 and 20, which share a return signal due to the loss of a return wire on channel 19. These channels appear to pick up the shield cooler compressor frequency of ~14 Hz causing 5% to 10% degradation in spectral resolution on these channels as shown in Fig. 10.

The two dominant spacecraft interference lines in the detector power-band are labeled in Fig. 7. The line at ~50 Hz is dominated by one of the four momentum wheels. In this case, the momentum wheel was operating around 3000 rpm when the noise spectra were accumulated. The line near 120 Hz is due to the magnetic torquer bars. The difference between the spacecraft thermal vacuum test and the in-flight performance summarized in Figs. 2 and 8 is largely due to modulation of these two effects as the spacecraft attitude control system is operated. We note that the effect is not large. A single 6-keV x-ray from ground testing and in-flight is shown in Fig. 8, and they are indistinguishable. The pulse analysis, however, uses an optimal filter[18] that essentially weights the frequency content of the pulse by the signal-to-noise ratio as a function of frequency. Since the amplitude, and in the case of the momentum wheels, the frequency of the interference is nonstationary, it cannot be effectively suppressed in the pulse analysis. Thus, the interference becomes a feature of the in-flight performance of the instrument, and this has been incorporated into the instrument response function.

We note that there is additional $1/f$ noise on channel 35, as shown in Fig. 7. This interference was not apparent in ground testing and did not appear until four days after launch. The noise spectra shown in Fig. 3 were taken 3 days after launch and the noise is not yet apparent. The additional noise did appear before the detectors were cooled to 50 mK suggesting the susceptibility is not in the detector housing but may be associated with the JFET amplifier or further up the electronics chain. The origin of the excess noise is not yet understood, although charged particle damage of the JFET channel is a possibility. The same JFETs were used on Suzaku (same production wafer), and there was no clear evidence of this effect on any of the 32 channels even after ~1 year on-orbit,[11] although we cannot yet exclude the possibility in this case. The excess noise appeared to be stable through the loss of the mission, causing ~1 eV of degradation in the performance (to ~5.9-eV FWHM) at 6 keV as shown in Fig. 10.

In Fig. 9, we show a comparison between the composite performance of the SXS detector system in three cases: during subsystem testing, during spacecraft thermal vacuum, and on-orbit. In Fig. 10, we show a similar comparison but on a per-pixel basis. Since the spacecraft interference is related to the attitude control system, this leads to a nonstationary effect on the instrument performance. The time dependence of the calibration pixel resolution is shown in Fig. 11. The time-dependent energy resolution correlated with the attitude control system as well as with cosmic rays interacting with the detector frame on-orbit, which is also time variable, varying with the magnetic rigidity.

3.4 *Gain Stability*

The SXS detectors utilize thermometers whose sensitivity is a very strong function of temperature. Thus if the detectors are operated at a different base temperature or with a different radiative load, the gain, i.e., the function that relates an x-ray pulse to the incident energy, can vary. For the SXS, this results in two components of the temporal variation in the gain: (1) a common-mode term where all the detectors respond similarly and (2) a differential term where the detectors do not have exactly the same response. The common-mode gain is valid for small

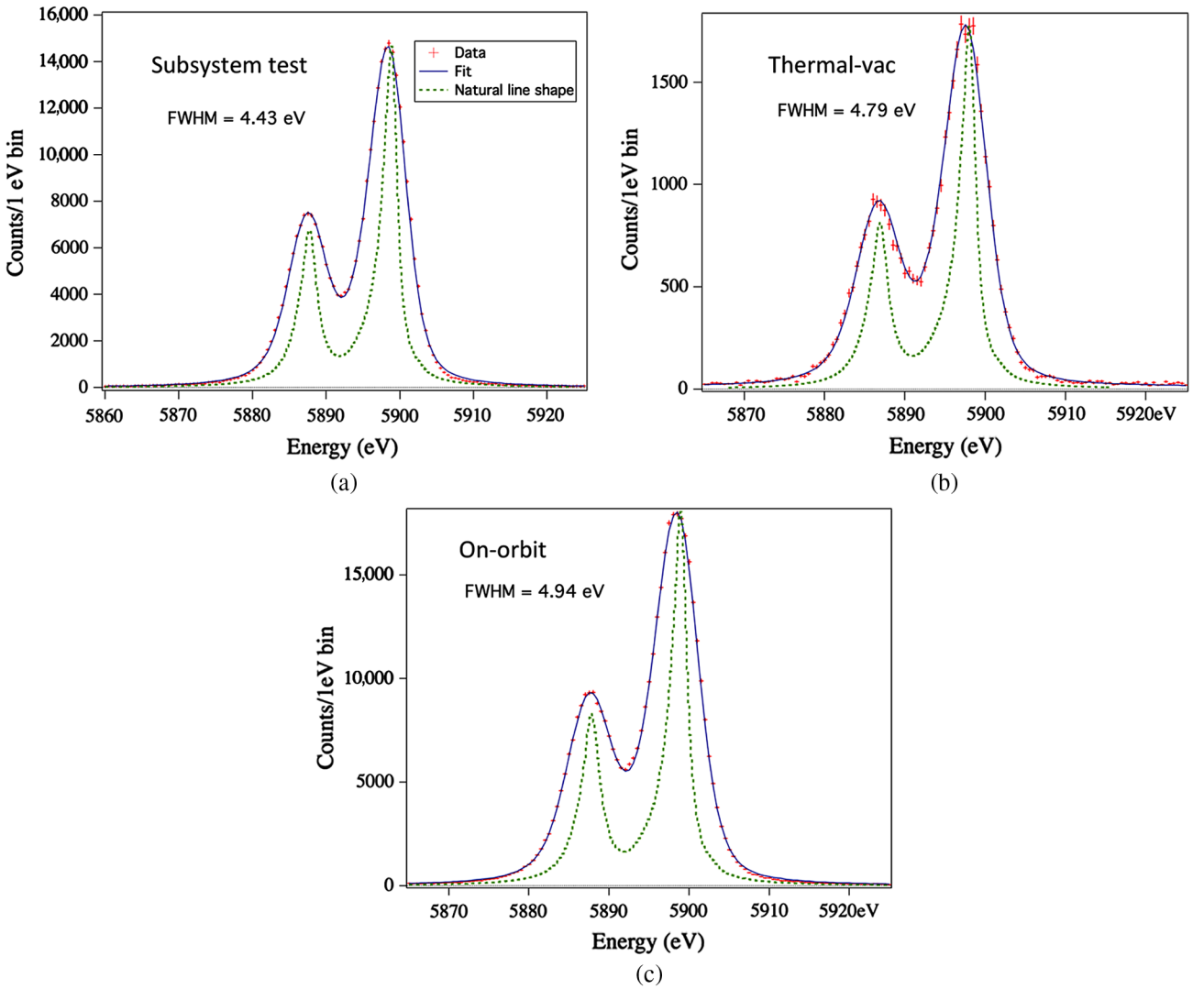

Fig. 9 SXS spectra of an external ^{55}Fe radioactive source during prelaunch tests and on-orbit. In each panel, the dashed line is the intrinsic line shape as measured by Hoelzer et al.,[19] and the difference between the data and the intrinsic line shape is the measured instrumental broadening. The results for the SXS FPA (a) before it was integrated into the SXS, (b) during full-spacecraft TVAC, and (c) is the result on-orbit. The differences are the result of a small amount of interference from the spacecraft attitude control system.

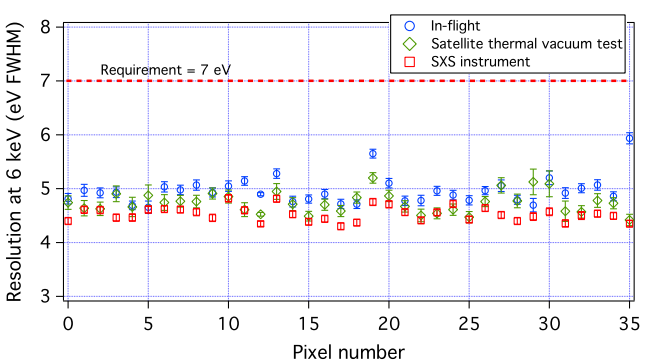

Fig. 10 Per-pixel energy resolution at 6 keV comparing the SXS instrument alone to the instrument on the spacecraft during TVAC and to the on-orbit performance. Note the anomalous degradation of pixel 35 on-orbit. This is related to an increase in $1/f$ noise on that channel as discussed in the text.

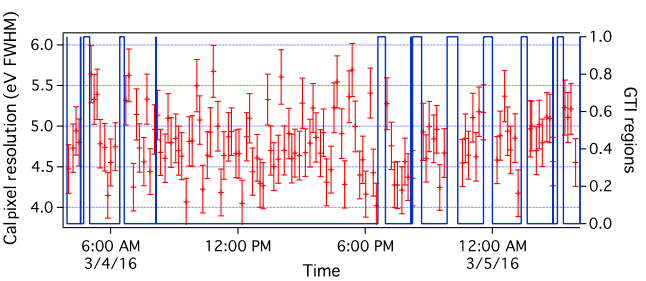

Fig. 11 Time dependence of the calibration pixel resolution (eV FWHM) at 6 keV for 10-minintegrations over a 24-h period on-orbit. The good-times intervals are shown by the solid line, marking the SAA intervals where the detector data are invalid (and not included in the data shown). The detector resolution is time variable, mostly, but not completely, correlated with interference from the attitude control system.

changes in the heat sink temperature and can be corrected by simply tracking the gain of the calibration pixel and imposing a correction factor across the array. For large temperature excursions or changes in radiative loading, there can be a substantial differential shift in the gain. In this case, a gain-tracking x-ray source is required for every pixel.

The SXS carries multiple calibration sources to track the gain on a per-pixel basis: a ^{55}Fe source mounted at a specific rotation of the external filter wheel and a modulated x-ray source (MXS), which is an electron bombardment source that can be turned on and off at a high rate. The MXS is especially useful since it can be gated out of the science data. With a suitable fiducial x-ray line, the detector gain and the resultant energy scale can be recovered to high precision. The process used for SXS is described by Porter et al.[20] However, early in the mission, only the internal calibration pixel was available for gain correction. There was also a single fiducial measurement with the external, filter wheel, ^{55}Fe source. The mission ended before the MXS could be fully energized. The science analysis, especially the early observations of the Perseus cluster,[3] used a bootstrap process of self-calibration coupled with the single fiducial measurement to calibrate the energy scale. The self-calibration process is described in Ref. 3, with some examples included below to illustrate the performance.

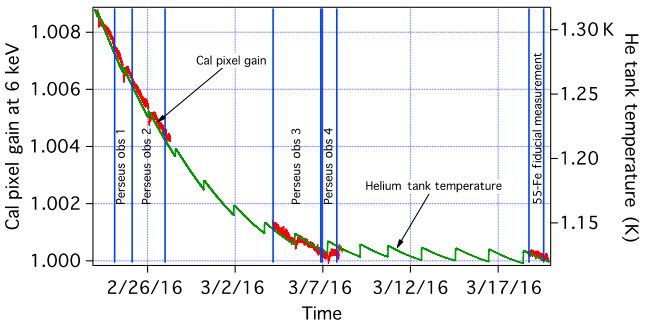

Fig. 12 Calibration pixel gain as a function of time starting 6 days after launch. The fractional gain (left axis) approximately follows the helium tank temperature that is the heat sink for the FPA structure (right axis). The staircase fluctuations in the He tank temperature are due to recycling the ADR. Some of the Astro-H observations are also indicated.

The gain error for the calibration pixel is shown in Fig. 12 as a function of time starting six days after launch. The gain approximately tracks the helium tank temperature (also shown). The helium tank temperature affects the gain due to conductive loading of the control thermometer, which causes the system to bias the detector housing heat sink temperature. This results in a common-mode gain error of the main detector array. The SXS pipeline software[21] tracks the calibration pixel and applies a temporal gain correction to the main array. However, there is also a differential gain term that must be corrected.

In Fig. 13, we show a portion of two Perseus cluster observations for a single pixel that observed the same position on the sky. The data have already been corrected for common-mode gain error using the pipeline analysis software and the calibration pixel. However, the gain continues to change during the observation especially during the first observation but also between the two observations. This illustrates the scale of the differential gain early in the mission. By the time the fiducial observation was made on March 19, the gain had largely stabilized and it is likely that very little gain tracking using the onboard calibration sources would have been necessary in later observations. For the Perseus cluster observations, the observation itself was used to correct the differential gain by tracking the position of the He-like Fe K_α line as a function of time and extrapolating to the full array fiducial measurement on March 19.[3] We note that the Perseus and other observations that were completed before the loss of the Astro-H mission were made before the instrument was fully deployed. In particular, the aperture gate valve was not yet open and the observations were made through a beryllium window. As discussed in Refs. 3 and 4, this restricted the effective area severely below 2 keV and by about a factor of 2 at 6 keV. We do not know

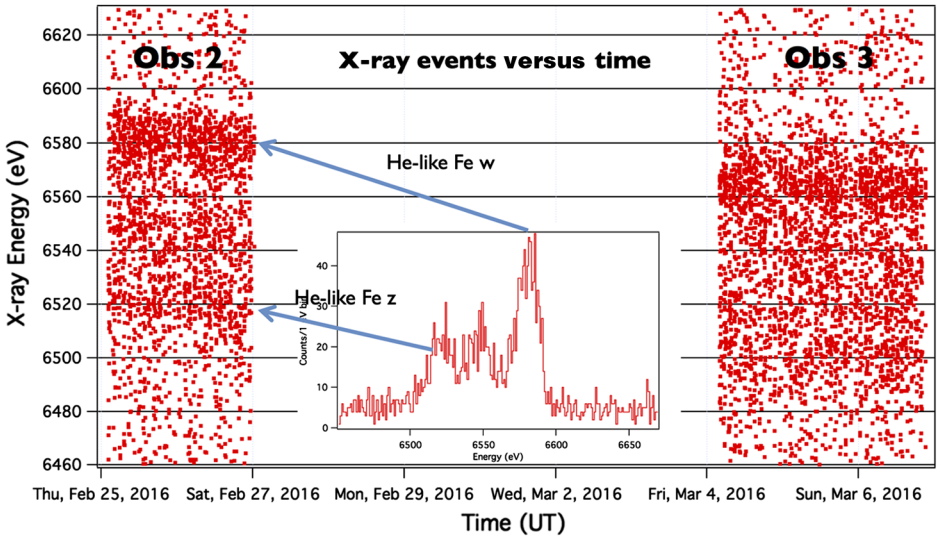

Fig. 13 X-ray energy versus time for a single SXS main array pixel for two Perseus observations shown in Fig. 12. Each point is a single x-ray event. For the data shown, the common-mode gain error has already been removed by the pipeline analysis software, but substantial differential gain error still remains. In later observations, the differential gain error was minimal as the system attained thermal equilibrium.

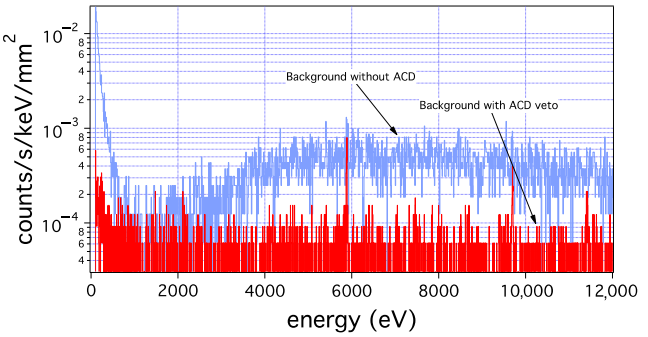

Fig. 14 SXS instrument background with and without a coincidence veto with the ACD.

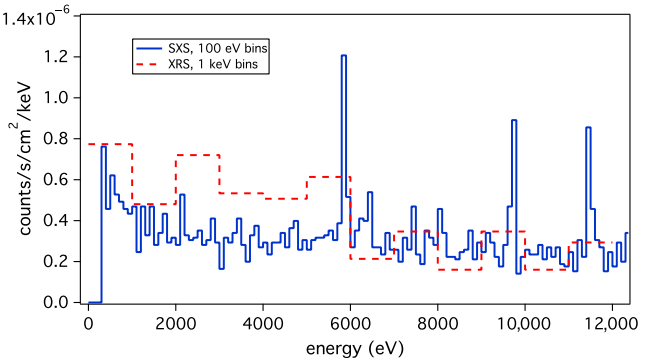

Fig. 15 A comparison of the non-x-ray background between the SXS instrument on Astro-H and the XRS instrument on Suzaku. Although the amount of data available from Suzaku is small, the results are very similar. Note that the prominent lines in the SXS spectrum are Mn K_α (5.9 keV) and Mn K_β (6.4 keV) scattered from the internal ^{55}Fe calibration source, and Au $L_{\alpha 1}$ (9.7 keV) and Au $L_{\beta 1}$ (11.4 keV) most likely from fluorescence of the detector heat sink.

whether this also provided additional RF shielding that may have masked other spacecraft interference on-orbit.

3.5 *Background*

The SXS FPA carried an ACD placed close behind the main array and operated at 50 mK.[13] The ACD is designed to effectively exclude high-energy particle interactions in the main array. The SXS telemeters all cosmic ray events interacting in the ACD to the ground and the veto timing with the main array occurs in the pipeline analysis software. The ACD is a single sided veto, and thus large angle events will not trigger both the ACD and the main array. However, minimum-ionizing particles at large angles produce events with energies outside the SXS bandpass and are discarded using an energy cut. In Fig. 14, we show an event spectrum of the main array during observations of blank sky. Blank sky was observed through a thin beryllium window in the closed instrument main-gate valve, effectively excluding the soft x-ray background. The residual background after the ACD veto is likely due to secondary particles and x-rays generated from primary cosmic rays within the SXS instrument. The residual background is consistent with that measured by the XRS instrument on Suzaku[11] as shown in Fig. 15.

Considerably, more background data were acquired with the SXS before the loss of the Astro-H observatory, and the detailed results are presented by Kilbourne et al.[22]

4 Summary

The SXS instrument and the SXS FPA performed nearly identically on-orbit compared to prelaunch testing and satisfied all of its performance requirements on-orbit. The array average energy resolution at 6 keV was 5 eV, a full 40% better than the 7-eV requirement. All subassemblies of the SXS performed nominally, including the bias system, the JFET amplifiers, the thermometry, and the ACD. The detector system is susceptible to temporal gain changes, especially during the very early phase of the mission when the instrument was far out of thermal equilibrium. This resulted in both common-mode and differential gain errors in the detector system. However, the common-mode error was effectively removed using the gain-tracking calibration pixel, and the differential errors had settled to nearly a constant value by the end of the mission and would have been effectively removed, as planned, with the on-board calibration sources.

There is considerable on-going analysis of the almost 6 weeks of Astro-H on-orbit data, both scientifically for the extant targeted observations, and for the performance of the instruments and spacecraft. For the SXS, a detailed study of the instrument background is underway. In addition, we continue to try to understand the small amount of spacecraft interference in detail and its implications for future missions, such as the planned X-ray Recovery Mission, which will refly the SXS instrument in 2022, and the much more complex Athena mission to fly in 2028.[23] We are also investigating the increase in $1/f$ noise in pixel 35 that led to a 20% decrease in the resolving power of that channel. In the end, however, the SXS performed nearly perfectly on-orbit before the untimely demise of the Astro-H observatory.

References

1. R. L. Kelley et al., "The ASTRO-H high-resolution soft x-ray spectrometer," *Proc. SPIE* **9905**, 99050V (2016).
2. T. Takahashi et al., "The ASTRO-H x-ray astronomy satellite," *Proc. SPIE* **9144**, 914425 (2016).
3. Hitomi Collaboration, "The quiescent intracluster medium in the core of the Perseus cluster," *Nature* **535**, 117–121 (2016).
4. R. Fujimoto et al., "Performance of the helium dewar and cryocoolers of ASTRO-H SXS," *Proc. SPIE* **9905**, 99053S (2016).
5. Y. Ishisaki et al., "In-flight performance of pulse processing system of the ASTRO-H soft x-ray spectrometer," *Proc. SPIE* **9905**, 99053T (2016).
6. P. J. Shirron et al., "Design and on-orbit operation of the adiabatic demagnetization refrigerator on the ASTRO-H soft x-ray spectrometer instrument," *Proc. SPIE* **9905**, 99053O (2016).
7. Y. Ezoe et al., "Porous plug phase separator and superfluid film flow suppression system for the soft x-ray spectrometer onboard ASTRO-H," *Proc. SPIE* **9905**, 99053P (2016).
8. M. Tsujimoto et al., "In-orbit operation of the ASTRO-H SXS," *Proc. SPIE* **9905**, 99050Y (2016).
9. Y. Takei et al., "Vibration isolation system for cryocoolers of soft x-ray spectrometer (SXS) onboard ASTRO-H," *Proc. SPIE* **9905**, 99050X (2016).
10. S. J. Smith et al., "Small pitch transition-edge sensors with broadband high spectral resolution for solar physics," *J. Low Temp. Phys.* **167**(3), 168–175 (2012).
11. R. L. Kelley et al., "The Suzaku high resolution x-ray spectrometer," *Publ. Astron. Soc. Jpn.* **59**, S77–S112 (2007).

12. C. A. Kilbourne et al., "The design, implementation, and performance of the ASTRO-H SXS calorimeter array and anti-coincidence detector," *Proc. SPIE* **9905**, 99053L (2016).
13. G. A. Sneiderman, "Cryogen-free operation of the soft x-ray spectrometer instrument," *Proc. SPIE* **9905**, 99053N (2016).
14. M. P. Chiao et al., "System design and implementation of the detector assembly of the ASTRO-H soft x-ray spectrometer," *Proc. SPIE* **9905**, 99053M (2016).
15. F. S. Porter et al., "The detector subsystem for the SXS instrument on the ASTRO-H observatory," *Proc. SPIE* **7732**, 77323J (2010).
16. M. E. Eckart et al., "Ground calibration of the ASTRO-H soft x-ray spectrometer," *Proc. SPIE* **9905**, 99053W (2016).
17. S. H. Moseley, J. C. Mather, and D. McCammon, "Thermal detectors as x-ray spectrometers," *J. Appl. Phys.* **56**, 1257–1262 (1984).
18. A. E. Szymkowiak et al., "Signal processing for microcalorimeters," *J. Low Temp. Phys.* **93**(3), 281–285 (1993).
19. G. Hoelzer et al., "K$\alpha_{1,2}$ and K$\beta_{1,3}$ x-ray emission lines of the 3d transition metals," *Phys. Rev. A* **56**(6), 4554–4568 (1997).
20. F. S. Porter et al., "Temporal gain correction for x-ray calorimeter spectrometers," *J. Low Temp. Phys.* **184**(1), 498–504 (2016).
21. L. Angelini et al., "ASTRO-H data analysis, processing, and archive," *Proc. SPIE* **9905**, 990514 (2016).
22. C. A. Kilbourne et al., "In-flight calibration of Hitomi soft x-ray spectrometer background," *PASJ* **70**(2), (2018), in press.
23. X. Barcons et al., "Athena: ESA's x-ray observatory for the late 2020s," *Astron. Nachr.* **338**(2–3), 153–158 (2017).

Frederick S. Porter is an astrophysicist at NASA's Goddard Space Flight Center, Greenbelt, Maryland. He received his BS degree in physics with honors from Harvey Mudd College in 1987. He received his ScM degree in physics in 1989 and his PhD in physics in 1993 from Brown University with a dissertation titled "Particle detection in superfluid helium." His current research interests include the soft x-ray background, interplanetary and magnetospheric charge exchange, and high-energy laboratory astrophysics.

Biographies for the other authors are not available.